

1 Surface Wave Measurement Based on Cross-correlation

2 Ge Jin¹ and James Gaherty¹

3 ¹ *Lamont-Doherty Earth Observatory, Columbia University*

4 SUMMARY

5 We developed a new method to retrieve the surface-wave phase velocity using dense seismic
6 arrays. The method measures the phase variations between nearby stations based on cross-
7 correlation. The phase variations are then inverted for the apparent phase velocity via Eikonal
8 equation. The amplitude measurements are performed on individual stations and are used to
9 correct the multi-pathing effect via Helmholtz equation. By using coherence and other data
10 selection criteria, we built up an automated system that retrieves phase velocity maps directly
11 from raw seismic waveforms without any human interactions. The system is tested on the
12 USArray data since 2006, and provides the weekly updated Rayleigh wave phase velocity
13 maps between the periods of 20 s and 100 s for the whole US. The results show significant
14 contrast between the tectonic active western US and the stable eastern US, as the phase velocity
15 variations in the western US are 1-2 times greater. The Love wave results are also calculated.
16 We find that the overtones contamination may produce systemic bias for the Love wave phase
measurements.

17 **Key words:** surface wave; phase velocity; automated; USArray; Rayleigh wave; US continent

18 1 INTRODUCTION

19 Seismic surface waves represent one of the primary means for scientists to probe the structure of
20 Earth's crust and upper mantle. Surface waves provide direct constraints on both absolute velocity
21 and relative velocity variations, and analysis of waves with different periods provides sensitivity
22 to different depths. These velocity variations in turn provide some of the best available constraints

2 *Ge Jin and James Gaherty*

23 on a variety of geodynamic parameters, including absolute and relative variations in temperature,
24 crust and mantle composition, the presence or absence of fluid (melt) phases, and the distribu-
25 tion and orientation of flow-induced mineral fabric. In many cases, however, resolution of these
26 properties is limited by uncertainties in observed surface-wave velocities due to complexity in the
27 seismic wavefield. Because they sample the highly heterogeneous outer shell of the Earth, surface
28 waves often contain the waveform complexity (Fig. 1) caused by focusing and defocusing effect
29 (often termed scattering or multipathing) that makes measurement of wave velocity uncertain.

30 In recent years, a number of investigators have developed data analysis schemes designed
31 to more robustly estimate surface-wave velocities in the presence of multipathing (Friederich &
32 Wielandt 1995; Forsyth & Li 2005; Yang & Forsyth 2006; Lin et al. 2009; Lin & Ritzwoller 2011;
33 Yang et al. 2011). These techniques exploit arrays of seismic stations to better quantify the detailed
34 character of the surface wavefield, specifically by combining measurements of both phase and am-
35 plitude between stations. These observations can be modeled in the context of wavefield character,
36 for example local plane-wave propagation direction (e.g. Forsyth & Li 2005) or apparent velocities
37 (Lin et al. 2009), as well as the structural phase velocity associated with the underlying media. The
38 techniques are particularly useful for estimating structural velocities in localized regions spanning
39 a receiver array, as opposed to along the entire path from the source to the receiver employed in
40 global (e.g. Levshin et al. 1992; Li and Romanowicz 1995; Ekström et al. 1997) and some regional
41 (e.g. Chen et al. 2007; Tape et al. 2010; Zhu et al. 2012) analyses. The estimates of structural phase
42 or group velocities across the array can then be inverted for models of seismic velocity through the
43 crust and mantle beneath the array, with greater confidence and accuracy than when using phase
44 information alone (e.g. Yang et al. 2011; Rau and Forsyth 2011; Lin et al. 2011).

45 We have developed a new algorithm to accurately estimate structural phase velocities from
46 broadband recordings of surface waves propagating across an array of receivers. The analysis is
47 based on the notion that waveform cross-correlation provides a highly precise and robust quantifi-
48 cation of relative phase between two observed waveforms, if the waveforms are similar in char-
49 acter. This notion is routinely exploited in body-wave analyses for structure (e.g. van Decar and
50 Crosson, 1990) and source (e.g. Schaff and Beroza, 2004) characteristics, but it is not widely

utilized in surface-wave analysis. Our approach builds upon the Generalized Seismological Data Functional (GSDF) analysis of Gee & Jordan (1992), which utilizes cross-correlation between observed and synthetic seismograms to quantify phase and amplitude behavior of any general seismic waveform, including surface waves (Gaherty & Jordan 1995; Gaherty et al. 1996; Gaherty 2004; Chen et al. 2007a; Chen et al. 2007b). By applying this quantification to cross-correlation functions between surface waves observed at two nearby stations, we generate highly robust and precise estimates of relative phase between the stations, due to the similar nature of the recorded waveforms. The procedure is applicable to arrays across a variety of scales, from the continental scale of EarthScope's USArray Transportable Array (TA), to the few 100's km spanned by a typical PASSCAL experiment, to 100's of meters in industry experiments, and is amenable to automated analyses with minimal analyst interaction. The resulting delay times and associated amplitudes can be modeled in the context of both wave-propagation and structural velocities. Here we outline the analysis, and demonstrate it's application to the TA array.

2 METHODOLOGY

2.1 Inter-station phase delays

The methodology is based on the GSDF work flow presented by Gee and Jordan, (1992), and subsequently utilized for regional upper-mantle and crustal modeling (e.g. Gaherty and Jordan 1995; Gaherty et al 1996; Gaherty 2001, 2004; Chen et al. 2007b; Gaherty & Dunn 2007). In those analyses, the starting point consists of an observed broadband seismogram containing all seismic phases of interest, and a complete synthetic seismogram relative to which the phase delays and amplitude anomalies can be measured. Here, we substitute a seismogram from a nearby station for the synthetic waveform, and measure phase and amplitude differences between interested phases recorded at the two stations. Waveforms from these two stations are presented as S_1 and S_2 here (Fig. 2). Because this is the first application of GSDF to an interstation analysis, we summarize the steps in some detail. Gee and Jordan (1992) provides a full theoretical presentation of GSDF.

The first step is to isolate the signal that we are interested in time domain. In the USArray application, we applied a window function W_S that includes the primary surface wave (Rayleigh on

4 Ge Jin and James Gaherty

78 vertical-component record, and Love on the transverse component) and most of its coda. Including
79 the coda is useful, in that it is often highly correlated at stations within 1-2 wavelengths, as shown
80 in Fig. 2. We then calculate the cross-correlation function $C(t)$ (cross-correlagram) between S_1
81 and $W_S S_2$, defined as:

82 $C(t) = S_1 \star W_S S_2$

83 $C(t)$ contains the delay or lag information of all coherent signals, with the peak corresponding
84 roughly to a wide-band group delay between the two stations, with a center frequency defined
85 by the dominant energy in the data, typically around 30 mHz for teleseismic Rayleigh waves.

86 We further isolate the dominant energy in the cross-correlation function in the time domain by
87 applying a Hanning window around the peak of the cross-correlation function, producing $W_c C(t)$.

88 The window function we applied here has a length of 200 s.

89 We then isolate the signals of interest in the frequency domain by convolving a sequence of
90 Gaussian, narrow-band filters with $W_c C(t)$, forming a set of filtered correlograms $F_i(\omega_i) * W_c C(t)$,
91 where $F_i(\omega_i)$ corresponds to each filter at center frequency ω_i (Fig. 3). These filtered correlograms
92 provide information of the frequency-dependent group and phase delays between the two stations,
93 as well as the coherence between the two signals. The frequency-dependent delays characterize
94 the relative dispersion that has occurred along the ray paths, and provide the fundamental data for
95 determining the phase velocity characteristics of the wavefield and the structure being sampled.

96 In the application that presenting 1 here, we are interested in characterizing the phase-velocity of
97 fundamental-mode surface waves in the 10-50 mHz band, and so we apply a sequence of 8 narrow-
98 band, zero-phase Gaussian filters with the band-width about 10% of the center frequency.

99 The narrow-band filtered cross-correlation function can be well approximated by a five-parameter
100 wavelet which is the product of a Gaussian envelope and a cosine function:

101 $F_i * W_c C(t) \approx AGa[\sigma(t - t_g)]\cos[\omega(t - t_p)]$

102 (Gee & Jordan 1992). In this equation, t_g and t_p represent the frequency-dependent group and
103 phase delays between the two stations, respectively, Ga is the Gaussian function, A is a positive
104 scale factor, σ is the half-bandwidth and ω is the center frequency of the narrow-band waveform. 

105 The raw phase and group delays can then be corrected for bias introduced by the time-domain
 106 windowing steps. As pointed out by Gee and Jordan (1992), windowing of the wide-band cross-
 107 correlation function around its peak introduces a bias in the frequency-dependent phase delays that
 108 can be estimated as:

$$109 \quad \delta t_{err} = (1 - \xi) \left[\frac{\omega_i - \omega_c}{\omega_i} (t_c - t_g(\omega_i)) \right]$$

110 where ξ is a time location parameter usually close to 1, ω_i is the frequency being measured, ω_c is
 111 the wide-band center frequency, t_c is center of the window function, $t_g(\omega_i)$ is the group delay of ~~frequency~~
 112 ~~frequency~~. This bias can be significant for those frequencies that are much lower than the center
 113 frequency, but can be minimized by iterating on the windowing and filtering process. In this study,
 114 for frequencies that are lower than 16 mHz (60 s), we utilize the initial estimate of ~~tg~~ to re-center
 115 the window function prior to narrow-band filtering these frequencies. This iteration procedure
 116 significantly reduces δt_{err} thereby minimizing the bias correction.

117 The raw phase delays are then checked and corrected for cycle-skipping. This is a particular
 118 important problem for the higher-frequency observations, and/or for station pairs with relatively
 119 large separation, for which the phase delay between the two stations may approach or exceed
 120 ~~multiple times of~~ the period of the observation, and the choice of cycle can be ambiguous. This
 121 problem is naturally avoided by only measuring the phase delay between the nearby station pairs.
 122 In the TA application, we only measure the station pair within 200 km, which is less than 3 wave-
 123 length of the shortest period (20 s). In ~~most~~ cases, a very rough estimation of reference phase
 124 velocity allows for unambiguous selection of the correct phase delay.

125 The window function W_S may also introduce bias in the measurement, simply by altering
 126 the input seismograms at the edges of the window. To account for this, we calculate the cross-
 127 correlation between S_2 and the isolation filter, $W_S S_2$.

$$128 \quad \tilde{C}(t) = S_2 \star W_s S_2$$

$$129 \quad F_i * W_c \tilde{C}(t) \approx \tilde{A} G a[\tilde{\sigma}(t - \tilde{t}_g)] \cos[\tilde{\omega}(t - \tilde{t}_p)]$$

130 Since S_2 and $W_S S_2$ are similar within the window of interest, $\tilde{C}(t)$ is similar to the auto-correlation
 131 function of $W_S S_2$ with the group delay and phase delay close to zero. Any non-zero phase change

6 Ge Jin and James Gaherty

132 measured in corresponds to a delay associated with the windowing process, and by assuming that
133 this windowing delay will be similar for the cross correlation $C(t)$, we calculate a final set of
134 bias-corrected delay times:

135 $\delta\tau_p = t_p - \tilde{t}_p$

136 $\delta\tau_g = t_g - \tilde{t}_g$

137 We perform this phase delay estimation between a given station and several nearby stations
138 generally those within 200 km. Fig 4 displays the raw phase delays for a representative event
139 recorded across the transportable array. These observed variations are driven primarily by struc-
140 tural variations beneath the array, and they form the basis for inverting for phase-velocity variations
141 across the array.

142 2.2 Wavefield amplitudes

143 The associated amplitude of the surface wavefield is estimated using amplitude measurements per-
144 formed on single station waveforms. As we have applied the five-parameter wavelet fitting to the
145 windowed and narrow-band filtered auto-correlation function $\tilde{C}(t)$ to remove the windowing ef-
146 fect in Section 2.1, it is convenient to use the scale factor \tilde{A} of the wavelet as a good approximation
147 of the power spectrum density function at center frequency of the narrow-band filter.

148 2.3 Derivation of apparent phase velocity

149 For each earthquake and at each frequency, the apparent phase velocity of the wavefield across the
150 array is defined by the Eikonal equation

151
$$\frac{1}{c'(\vec{r})} = |\nabla\tau(\vec{r})|$$

152 where $\tau(\vec{r})$ is the phase travel time. Also called the dynamic phase velocity, $c'(r)$ is the reciprocal
153 of travel time surface gradient, which is close to the structural phase velocity, but will likely be dis-
154 torted by propagation effects such as multi-pathing, back-scattering, and focusing of the wavefront
155 (Lin et al. 2009). The collection of inter-station phase delays provides a large and well-distributed

156 dataset for estimating the phase gradient via tomographic inversion. The phase difference between
 157 two nearby stations $\delta\tau_p$ can be described as:

$$158 \quad \delta\tau_p = \int_{r_i} \vec{S}(\vec{r}) \cdot d\vec{r}$$

159 where $\vec{S}(\vec{r})$ is the slowness vector and \vec{r}_i is the great-circle path connecting the two stations. We
 160 invert for the two orthogonal components of the slowness distribution (S_R and S_T) as a function
 161 of position across the array. S_R follows the great-circle path direction from the epicenter, and is
 162 positive in most cases. S_T is orthogonal to S_R with usually a much smaller value, and can be either
 163 positive or negative depending on the real direction of wave propagation.

164 The inversion is stabilized using a smoothness constraint that minimizes the second order
 165 derivative of S_R and S_T . The error function being minimized can be presented as:

$$166 \quad \varepsilon_c^2 = \sum \left| \int_{r_i} \vec{S}(\vec{r}) \cdot d\vec{r} - \delta\tau_{p_i} \right|^2 + \lambda \left(\sum |\nabla^2 S_R|^2 + \sum |\nabla^2 S_T|^2 \right)$$

167 where the first term is the difference between observed and predicted phase delay, and λ is a factor
 168 to control the smoothness. The upper left panel of Fig 5 presents the apparent (Eikonal) phase
 169 velocities determined from the $\delta\tau_p$ data presented in Fig 4.

170 2.4 Derivation of structural phase velocity

171 The bias between apparent phase velocity and structure phase velocity can be corrected by adding
 172 amplitude measurements into the inversion, using an approximation to the Helmholtz equation
 173 (Wielandt 1993; Lin & Ritzwoller 2011):

$$174 \quad \frac{1}{c(\vec{r})} = \frac{1}{c'(\vec{r})} - \frac{\nabla^2 A(\vec{r})}{A(\vec{r})\omega^2}$$

175 Here $c(\vec{r})$ is the structural phase velocity and $A(\vec{r})$ is the amplitude field. The amplitude Laplacian
 176 term corrects for the influence of non-plane wave propagation on the apparent phase velocities,
 177 allowing for the recovery of the true structural phase velocity. Lin and Ritzwoller (2011) applied
 178 this formulation to USArray data to explore the seismic structure of the western US. The input ap-
 179 parent phase velocity $c'(\vec{r})$ is derived as in Section 2.3. For the amplitude term, we follow Lin and

8 Ge Jin and James Gaherty

180 Ritzwoller (2011) by fitting a minimum curvature surface to the single-station amplitude estimates
181 from Section 2.2. The error function for the surface fitting is:

$$182 \quad \varepsilon_A^2 = \sum_i |A(r_i) - A_i|^2 + \gamma \sum |\nabla^2 A(\vec{r})|^2$$

183 where A_i is the observed station amplitude at location r_i , $A(r_i)$ is the interpolated amplitude es-
184 timated at r_i , and γ controls the smoothness of the surface. In practice, calculating the second
185 gradients of this amplitude field $A(\vec{r})$ is sometimes problematic, as the Laplacian operator magni-
186 fies short-wavelength noise, and individual amplitude measurements can be highly variable due to
187 local site conditions and erroneous instrument responses. We utilize a finite difference calculation
188 to estimate the second derivative numerically, and then one more step of smoothing is performed
189 on the correction term to suppress the short-wavelength noise (Fig. 14, see Section 5.2 for more
190 details).

191 The amplitude correction cannot be simply applied on Love wave measurements, as the phase
192 and amplitude measurements of Love wave are taken on the tangential component of the great
193 circle path direction, which is not necessarily to be the particle motion direction of the propagating
194 Love wave field. The present of multi-pathing wave fields makes the situation more complicated,
195 in which the Helmholtz equation is not justified. As a result, all the Love wave results shown and
196 discussed in this paper are Eikonal tomography results.

197 In the following section, we present the full application of this analysis to data from USArray.
198 The analysis up through the calculation of structural phase velocity is done for individual events,
199 and a range of frequencies. For a fixed array geometry, the resulting phase-velocity maps from
200 individual events are averaged (stacked) to produce the final phase-velocity maps that can be used
201 in a structural inversion for shear velocity. In the case of a rolling array such as the TA, stacking
202 and averaging over multiple events produces a single comprehensive phase-velocity map that spans
203 the history of the array deployment.

204 **3 DATA PROCESSING AND AUTOMATION**

205 We have applied our method on the data of USAArray since 2006. The software SOD (Owens et
 206 al. 2004) is used to download the seismic waveforms and to remove the instrument response, and
 207 Matlab is used to realize other operations. In the process of building up the program, we reduced
 208 the human interaction as much as possible to minimize the subjectivity of the measurement.

209 **3.1 Auto generation of isolation filter**

210 As the first step of the whole process, a window function W_S is required to isolate the fundamental
 211 mode energy of surface wave. The desired window function W_S should be wide enough to include
 212 the arrivals of the maximum amplitudes of all frequencies, and narrow enough to eliminate the
 213 interference from other phases like higher modes and body waves.

214 To generate this window function, we first estimate the group delays of all the frequency bands
 215 at individual stations using the FTAN method (Levshin et al. 1992). The time-range to be included
 216 for each frequency is two cycles before and five cycles after the group delay. At each station, we
 217 select the first beginning and last ending time among these time-ranges of all the frequency bands,
 218 and define them as the beginning and ending time of the suggested window function of the station.

219 As the single station group delay measurements are highly variable, we collect the locations of
 220 the suggested window functions for the whole array, and regress a linear relation between the time
 221 range of the final window function W_S and epicenter distance. The relation is defined as:

$$222 \quad T_1 = \frac{L}{v_1} + t_1$$

$$223 \quad T_2 = \frac{L}{v_2} + t_2$$

224 where T_1 and T_2 are the beginning and ending time of W_S , L is the epicenter distance, and v_1, v_2 ,
 225 t_1, t_2 are the parameters estimated by the linear regression.

226 An example of automated window selection is shown in Fig. 1.

227 **3.2 Auto selection of good measurements**

228 We have designed three independent strategies to exclude unqualified phase measurements auto-
 229 matically at different stages of the data processing.

230 We first use coherence between the waveforms of nearby stations as the most important factor
 231 to eliminate measurements with low signal-to-noise ratio (SNR) or from dysfunctional stations.
 232 The coherence is frequency dependent and can be estimated by comparing the amplitude of cross-
 233 correlation function $C(t)$ and two auto-correlation functions $\tilde{C}(t)$. Since we have already fit the
 234 five-parameter wavelet to those functions, it is convenient to use those fitting results. Coherence at
 235 a certain frequency can be written as:

$$236 \quad \gamma = \frac{A_{12}^2}{\tilde{A}_{11}\tilde{A}_{22}}$$

237 where A_{12} is the amplitude of narrow-band cross-correlation wavelet estimated in the section 2.1,
 238 \tilde{A}_{11} and \tilde{A}_{22} are the amplitudes of the narrow-band auto-correlation wavelet of the two stations
 239 estimated in the section 2.2. In this study, we exclude all the measurements with the coherence
 240 lower than 0.6.

241 The second round of data selection is performed after the phase delay measurements from all
 242 the station pairs are gathered. We estimate the average phase velocity at each frequency by linear
 243 fitting the phase delay with epicenter distance difference. Then the measurements with misfits
 244 more than 10 s from this linear regression are removed. 10 s is a weak constrain, as most of
 245 the heterogeneities in the US continent only produce phase delay anomalies less than 5 s from the
 246 average phase velocity prediction between the station pairs that are less than 200 km apart (Fig. 4).
 247 This simple treatment discards most of the extreme measurements and thus stabilizes the following
 248 Eikonal inversion.

249 Finally, after the Eikonal inversion described in Section 2.3 is done, we reject the measure-
 250 ments with the inversion misfit larger than three standard deviations, and invert the slowness again.
 251 This step removes the inconsistent measurements and enhance the robustness of apparent phase
 252 velocity results.

253 For the amplitude measurements, we discard the stations with the amplitude variation larger
 254 than 30% of the median amplitude of their nearby stations (<200 km).

255 **4 RESULTS**

256 Based on the techniques described above, we developed an automated system to retrieve the sur-
 257 face wave phase velocity maps directly from the USArray waveform data. Once a week the system
 258 is activated to download the broadband waveforms of eligible earthquakes ($M_s > 6.0$, depth < 50
 259 km), and to process the data to generate tomographic maps as shown in Fig. 5. The structural phase
 260 velocity maps from individual earthquakes are then weighted and stacked. The weighting of each
 261 pixel in the phase velocity maps for each earthquake is based on the ray density in the slowness
 262 inversion described in Section 2.3.

263 **4.1 Comparison with ambient noise results**

264 Micro-seismic generated ambient noise has been widely used to retrieve surface wave phase ve-
 265 locity at high frequencies (e.g., Bensen et al. 2007). We here compare the earthquake phase
 266 velocity results from this study at the highest frequencies with the ambient noise results pro-
 267 vided by Ekström (2013). These ambient noise results are also the output of an automated sys-
 268 tem, which downloads the continuous waveform data, estimates and stacks the normalized co-
 269 herence, retrieves phase delays between station pairs in the frequency domain (Ekström et al.
 270 1997), and regulates phase velocity maps using ray theory. The results are regularly updated and
 271 can be downloaded from the author's website (<http://www.1deo.columbia.edu/~ekstrom/>
 272 Projects/ANT/USANT12.html).

273 Fig. 7 illustrates the comparison for Rayleigh waves and Love waves at a period of 20 s. It
 274 can be seen that the results are highly consistent, despite they are retrieved from different seismic
 275 sources by using different phase measurement techniques and velocity inversions. Strong geolog-
 276 ical features are clearly highlighted in both results, while the greater inconsistency (Fig 7c and f)
 277 near the west coast and other strong velocity contrasts may result from different smooth damping.

278 Fig. 8 shows the statistic summary of this comparison. For Rayleigh wave, the correlation

12 *Ge Jin and James Gaherty*

279 coefficient between the two maps is 0.94. The mean and the standard deviation of the velocity
280 difference are 0.018 km/s and 0.030 km/s, respectively. The small but systemic difference shows
281 slightly higher velocities (0.5%) from this study, which demonstrates¹ the influence of the finite
282 frequency effect¹, as the Helmholtz tomography allows for ray bending while conventional ray
283 theory does not.

284 The Love wave results are usually less robust because of the higher noise level in the horizontal
285 components. Nevertheless, the correlation coefficient between the two studies is 0.89. The mean
286 and the standard deviation of the velocity difference for Love waves is 0.035 km/s and 0.050
287 km/s, respectively. A larger systemic difference is observed (0.9%), which is almost twice the
288 value of the difference in the Rayleigh wave results. We will discuss this bias in more detail in the
289 Section 4.2.3.

290 We also compare the results at two longer periods (25s and 40 s). The means and standard
291 deviations of the differences are summarized in Fig. 9. For Rayleigh waves, we find the difference
292 between the two studies are small. The correlation coefficients range from 0.944 to 0.966 with
293 slightly increase with period. For Love waves, on the other hand, the systemic bias between the
294 earthquake and the ambient noise measurements increases significantly with period, from 1% at
295 20 s period to 3% at 40 s period. And¹ the correlation coefficients drop¹ from 0.891 at 20 s period to
296 0.780 at 40 s period. We suspect that this bias is mainly controlled by the overtones² interference,
297 which will be discussed in more details in the Section 4.2.3.

298 **4.2 Possible Source of Error**

299 *4.2.1 Station Terms*

300 Although the automated data selection techniques described in Section 3 are able to eliminate
301 most of the unqualified measurements with low SNR, they cannot distinguish the stations with a
302 time-shift problem or an abnormal amplification term, as the waveforms of those stations may still
303 correlate well with their neighbors².

304 The station time-shift can be generated either from GPS¹ dysfunction or from the incorrect
305 instrument response, which results the timing of the station a bit earlier or later comparing to other

306 stations. The stations with time-shift can be distinguished in the apparent phase velocity maps
 307 by generating two short-wavelength anomalies with reversed polarization. The anomalies usually
 308 locate before and after the station location on the direction of wave propagation. Those stations
 309 can be manually identified and excluded. We do not perform this manual selection in this study,
 310 because we want to demonstrate the results of a fully automated system.

311 The station amplification term, on the other hand, is more unavoidable and with less obvious
 312 influence comparing to the time-shift problem. The amplitude correction we apply in Section 2.4 is
 313 based on the assumption that all the stations have the same amplification term, which is not perfect
 314 as the station amplification term can be affected by local geological structures and installation
 315 conditions. The ideal way to eliminate this bias is to first estimate the station amplification term by
 316 averaging multiple events (Eddy & Ekström 2013), or to invert the phase velocity and amplification
 317 term iteratively (Lin et al. 2012). However, the amplification term of most stations in the USArray
 318 is very close to 1 (Eddy & Ekström 2013), so their influence on the final results is minor.

319 4.2.2 Azimuthal Anisotropy

320 Several studies (e.g., Lin et al. 2011) have reported the existent 1-2% of Rayleigh wave azimuthal
 321 anisotropy in the western and central US. The azimuthal anisotropy can be estimated by fitting the
 322 structural phase velocity with the wave propagation direction obtained in the slowness inversion.
 323 However, in this study, we stack the results from well distributed events to minimize the influence
 324 of the azimuthal anisotropy, as there are not enough data yet in the east part of the array to perform
 325 the inversion. The azimuthal anisotropy inversion will be included in the future studies when the
 326 TA project has fully covered the US continent. 

327 4.2.3 Overtones Interference

328 We do not observe any significant effects of higher modes interference on the Rayleigh wave phase
 329 velocity maps, as no significant bias is found between the earthquake and the ambient noise re-
 330 sults (Fig. 9). The source of ambient noise is usually believed to be shallow, and therefore the
 331 amplitudes of overtones are relatively smaller in the ambient noise waveforms than in the earth-

quake waveforms. If we assume that the ambient noise result is overtone-free, the consistency between the earthquake and the ambient noise result for Rayleigh waves indicates that the effect of overtones interference is small.

For Love waves, the effect of overtones interference on the phase measurement is more significant than for Rayleigh waves, as the group velocity difference between the Love-wave fundamental mode and overtones is smaller. Although we choose only the shallow events (<50 km) to be measured, as they excite less overtones energy, the comparison between the earthquake and the ambient noise results still shows a significant frequency-dependent systematic bias (Fig. 9).

Foster et al. (2014a) reported a systematic higher phase velocity obtained from the mini-array method (similar to Eikonal tomography) than from the long-path two-station method. The bias they found for the 50-s Love wave has a similar magnitude as the bias we observed for the 40-s Love wave. A follow-up study (Foster et al. 2014b) suggested that the overtones interference affects the methods using local phase gradient measurements more than those using long ray-path measurements, and the bias generated by this influence can be systematic.

The group velocities of the Love wave fundamental mode and the first mode behave differently in the oceanic structure and continental structure (Nettles & Dziewoński 2011). In the ocean, these two modes propagate at a very similar speed, so it is difficult to distinguish them in the time domain. In the continent, on the other hand, the group velocity of the fundamental mode drops dramatically at higher frequencies (>20 MHz), while the group velocity of the first mode remains high. In general, for the continental stations, the time difference between the group delays of the fundamental mode and overtones is larger at higher frequencies, so less overtones interference will affect the phase measurement. This explains the observation in Fig. 9, with the bias between the earthquake and the ambient noise results increase with frequency.

Moreover, how the phase is measured also determines the amplitude of the bias. In general, when applying the window function on the original waveform to isolate the surface wave energy, the methods that apply different window functions at different frequencies (e.g. Levshin et al. 1992, Ekström et al. 1997) are less biased at higher frequencies (>25 mHz) than the methods that use the same window function at all frequencies (e.g., this study, Forsyth & Li 2005). However, as

360 the group delay between the fundamental mode and higher modes become closer and the envelop
 361 of the wavelets become boarder at lower frequencies, all the methods are affected and biased.

362 Because the Love wave results are contaminated by overtones interference and hence system
 363 biased, they are not presented in this paper. ~~The effect of overtones interference on the Love wave~~
 364 phase velocity results will be further investigated, yet it is beyond the scope of this study.

365 4.3 Phase Velocity Maps

366 From 2006 to 2014, totally ??? cross correlation measurements from ??? earthquakes are inverted
 367 for structure phase velocities of both Rayleigh wave and Love wave in 8 frequency bands. The
 368 Rayleigh wave results are shown in Fig. 6. The results of Love wave are calculated but not shown
 369 in this study because of the overtones contamination.

370 Due to the various data lengths and qualities, the number of events being stacked at each pixel
 371 varies at different locations and frequencies. Only the pixels averaging more than 10 events are
 372 shown in the maps. After the stacking, the phase velocity maps are further smoothed based on
 373 their average wavelength at each frequency.

374 4.4 Spectral Analysis of the Phase Maps

375 We apply the 2D Fourier transform analysis on the Rayleigh wave phase velocity maps to investi-
 376 giate the amplitude of phase velocity variations at different structural wavelengths and different
 377 frequencies. We separate the western and the eastern US in this analysis to compare the tectonic
 378 active and tectonically stable parts of the continent.

379 The Fourier transform is performed in the sinusoidal map projections centered at $(40.5^\circ, -113^\circ)$
 380 and $(38^\circ, -90^\circ)$ for eastern and western US respectively. ~~The regions are marked in Fig. 10a. We~~
 381 ~~interpolate the pixels without results by using the minimum curvature surface interpolation,~~ and
 382 subtract the average phase velocity from each map to focus on the velocity variations. The varia-
 383 tion amplitude spectra are shown in Fig. 10b. They illustrate the phase velocity variations for the
 384 structures with different wavelengths. Only the structural wavelengths that are larger than the sur-

385 face wave wavelengths are plotted to ensure the results are well within the resolution, and the
386 variation amplitude is not biased due to the sampling by different surface wave wavelengths.

387 The spectra of both western and eastern areas (Fig.10b) indicate an increase of the variation
388 amplitudes with the structural wavelengths, which is consistent with the trend of the global obser-
389 vation at a larger scale (Dziewoński et al. 2010). This observation also agrees with the common
390 sense that it is usually difficult to maintain a strong anomaly (either compositional or thermal)
391 within a short wavelength.

392 In the western US, the variation amplitudes measured at the shortest periods (20 s and 25 s)
393 are in general much stronger than the variation amplitudes at longer periods. This trend is visible
394 but less obvious in the eastern US. The phase velocity in high frequency bands is more likely to be
395 affected by the depth of Moho, which is the most significant velocity gradient in the lower crust
396 to the upper mantle depth range. The rough topography of Moho in the western US (Shen et al.
397 2013) may enhance the phase velocity variations at high frequencies. In the eastern US, on the
398 other hand, the Moho depth variation may be smaller due to the less significant phase velocity
399 variations at high frequencies.

400 On average, the variation amplitudes in the western US is 1-2 times greater than those in
401 the eastern US at most wavelengths. The long-existing geological structures (e.g., mid-continent
402 rift system, Grenville Oregon, Piedmont plateau) indicate an active tectonic history in the eastern
403 US, which should have generated strong seismic velocity anomalies with a magnitude similar to
404 those in current western US. While the tectonic staying stable for hundreds of million years, the
405 amplitude of these velocity anomalies has decreased significantly mainly due to two mechanisms:
406 thermal diffusion and gravity isostasy. The thermal diffusion makes the temperature field in the
407 upper mantle more isotropic, which reduces the phase velocity variation at lower frequencies;
408 and the gravity isostasy together with the surface erosion smoothen the Moho topography, hence
409 decrease the phase velocity variation at high frequencies.

410 **5 DISCUSSION**

411 **5.1 Improvement comparing to FTAN method**

412 In this section, we would like to compare the cross correlation method developed in this study with
 413 the conventional Frequency Time Analysis (FTAN) method developed by Levshin et al. (1992).

414 The FTAN method is widely used in many global or regional surface wave studies (e.g. Lev-
 415 shin et al. 1992; Levshin & Ritzwoller 2001; Lin & Ritzwoller 2011; Yang et al. 2011). This
 416 method applies a sequences of narrow-band filters to the raw seismograms, and retrieves the group
 417 delay at each frequency by tracking the arrival time of envelop function maximum. The phase
 418 and amplitude measurements are then made at these amplitude maximums for later tomographic
 419 inversion. Although theoretically the two methods extract the same information from data, they
 420 behave slightly differently in the real situation.

421 First, the two methods exploit different techniques to retrieve phase: this study performs cross-
 422 correlation on coherent signals between stations to obtain the relative phase variation, and the
 423 FTAN method applies Hilbert transform of single-station waveforms to retrieve absolute phase
 424 value. Cross-correlation can suppress the influence of random noise, which is not coherent among
 425 the stations, and therefore makes the measurements with low SNR more robust. Here we propose
 426 a simple 1D synthetic test to demonstrate the effect of random noise on both methods. A narrow-
 427 band wavelet propagating along a straight line is simulated by a cosine function enveloped by a
 428 Gaussian function. The group velocity of the wavelet (the velocity of Gaussian envelop) is 3.7
 429 km/s and the phase velocity is 4.0 km/s. We add a normal distributed random noise to the data.
 430 The standard deviation of the added noise equals to 20% of the wavelet's maximum amplitude.
 431 We then measure the phase velocity between 500 station pairs using both methods. The station
 432 spacing between two stations is 50 km along the ray path. A summary of this comparison is shown
 433 in Fig. 11. The result shows that under the same noise level, the standard deviation of cross-
 434 correlation measurements is significantly smaller (50%) than that of the FTAN measurements.

435 Second, the two methods are sensitive to different portion of data. The FTAN method only
 436 samples the waveform near the group delay at each frequency, where the surface wave has biggest

amplitude. However, selection of the group delay can be difficult at higher frequencies, as multiple local maximums with similar amplitude may exist in the envelop function due to strong scatter effect and high noise level (Fig. 12). Each local maximum, or wavelet, represents an individual propagation path. Thus selecting inconsistent wavelets through the array introduces bias into the later phase velocity inversion. In contrast, our method cross-correlates the whole surface-wave package, which includes the first arrival and the coda generated by the heterogeneity along the ray path. The phase measurement we make is thereby the result of multi-pathing wavelets interference, which can be corrected by amplitude measurement to obtain structure phase velocity. In practice, our method can retrieve robust phase velocity at a period as short as 20 s from earthquake data. On the other hand, cross correlating a larger portion of the waveforms and adopting the same window function for all frequency bands also result more overtones energy being included into the measurement for Love waves. Please see Section 4.2.3 for more details.

Fig. 13a and b demonstrate the performance of the two methods for a real earthquake. Fig. 13a is the reproduced apparent phase-velocity map of Rayleigh wave by following the algorithm described in Lin & Ritzwoller (2011), which is basically the same result as shown in the fig.4a of their paper. In the Fig. 13b, we replace the FTAN phase measurements with our cross-correlation measurements and keep the velocity inversion the same as Fig. 13a. The comparison between the two plots indicates that our method substantially reduces short-wavelength noises in apparent phase velocity inversion, and provides more stable measurements at low amplitude stations compare to the FTAN method.

5.2 Helmholtz Tomography

Another purpose of this study is to provide alternative ways to realize Eikonal and Helmholtz tomography developed by Lin et al. (2009) and Lin & Ritzwoller (2011).

Because phase variance between stations instead of absolute phase at individual station is measured, we avoid reconstructing the travel time surface $\tau(\vec{r})$ and then taking its gradient to obtain apparent phase velocity. Instead, we prefer to invert the orthogonal components S_R and S_T of the slowness vector directly. This notion provides several advantages. First, we can use

the well developed ray theory techniques to build up the inversion. Second, like conventional ray theory tomography, the ray density serves as a valuable proxy that quantitatively indicates the reliability of the inversion constrained by data. It can be used to determine the pixels with reliable result and to weight the later averaging process. Third, by putting the smoothing kernel on slowness instead of its integral (travel time), we gain better control on the smoothness of the desired variable. Minimizing the second derivative allows the slowness to vary smoothly, while fitting the minimum curvature travel time surface leads to minimizing the slowness variation. Finally, constraining the smoothness along the radial and tangential directions of the great circle path is more natural for the 2D propagating wave field than along the latitude and longitude direction. It does not make much improvement for the far-field measurements as in this study, but may help the near-field surface fitting for the ambient noise study as in Lin et al. (2009).

Fig. 13b and c shows the results of the two different kinds of Eikonal tomography inversion on the same phase measurements. Comparing to Fig. 13b, Fig. 13c indicates that by using the slowness inversion, the short wave length noise is further suppressed while the variation magnitude of the strong anomalies (e.g. Yellow Stone hot-spot and Rocky Mountain) are maintained. This improvement has the potential to enhance the resolution of final results, though it is secondary comparing to the improvement we obtain from the cross-correlation phase measurement (Fig. 13).

To obtained the amplitude correction term is more challenging. First of all, amplitude measurement is not as robust as phase measurement. Both our method and the FTAN method estimate amplitude based on single station measurement, which is difficult to control the measurement quality. Surface wave amplitude is also affected by local amplification and station term (Lin et al. 2012; Eddy & Ekström 2013). Moreover, the correction term relies on the estimation of the amplitude Laplacian term. Using finite difference to calculate the second-order derivative of a surface at a certain location requires 9 to 16 adjoint data points, which triples the requirement to obtain the gradient. For an array setup like USAarray with 70-km average station spacing, this restricts the resolution of the amplitude correction term to be lower than 140 km (Lin & Ritzwoller 2011). Last but not least, fitting amplitude surface by minimizing its curvature does not guarantee the smoothness of its Laplacian term, as shown in Fig. 14b. Adding fourth order derivative minimization into

492 the damping kernel to fit the amplitude surface was attempted, but no significant improvement was
 493 observed.

494 To partially resolve these difficulties, we adopt ~~an approach that is similar to but slightly differ-~~
 495 ~~ent from~~ Lin & Ritzwoller (2011). After retrieving the amplitude surface (Fig. 14a) and calculating
 496 the second derivative, a rough correction term is generated ~~first~~ (Fig. 14b). We then fit a minimum
 497 curvature surface again over this preliminary correction term, with a much larger damping factor
 498 to remove any variance with the wavelength shorter than the theoretical resolution (140 km for
 499 USArray), as shown in Fig. 14c. The smoothed correction term can then be applied to clean up
 500 the apparent phase velocity map. By comparing Fig. 14d and Fig. 13c, we can see that the bias
 501 resulted by multi-pathing interference is significantly reduced and the shapes of the anomalies are
 502 more consistent with the geological structures.

503 5.3 Compatibility with the two-plane-wave method

504 The two-plane-wave method (TPWM) (Forsyth & Li 2005) ~~is more conventional than the Eikonal/Helmholtz~~
 505 ~~tomography method (Lin et al. 2009; Lin & Ritzwoller 2011)~~ in the field of surface wave tomog-
 506 ~~raphy. It shows more advantages for small array configuration with irregular station spacing. The~~
 507 ~~TPWM retrieves amplitude and phase information at individual stations using Fourier transform,~~
 508 ~~and requires the data with low quality to be manually discarded.~~ In this section, we provide a sim-
 509 ple algorithm to convert the cross-correlation measurements into a format that can be used as the
 510 input of the TPWM.

511 The TPWM requires the relative phase delays of all stations compare~~to~~ a reference station.
 512 The cross-correlation measurements provide the ~~relative phase variance~~ between the station pairs.
 513 Each phase difference measurement can be written as:

$$514 \quad \tau_i - \tau_j = \delta\tau_{ij}$$

515 Where τ_i and τ_j represent the absolute phases at station i and station j, and $\delta\tau_{ij}$ is the cross-
 516 correlation phase difference measurement ~~we perform~~ in this study. To solve τ_i , a matrix formula
 517 $A\tau = \delta\tau$ is built as:

$$518 \quad \begin{pmatrix} 1 & -1 & 0 & \dots \\ 1 & 0 & -1 & \dots \\ 0 & 1 & -1 & \dots \\ \vdots & \vdots & \vdots & \vdots \end{pmatrix} \begin{pmatrix} \tau_1 \\ \tau_2 \\ \tau_3 \\ \vdots \end{pmatrix} = \begin{pmatrix} \delta\tau_{12} \\ \delta\tau_{13} \\ \delta\tau_{23} \\ \vdots \end{pmatrix}$$

519 Where the matrix A on the left side is redundant but not full rank, as no absolute phase information of any station is given. At this point we need to add one more equation to the set:

521 $\tau_1 = 0$

522 by assuming the first station (can be any station in the array) has zero phase. Then the matrix A is
523 invertible, and the problem can be solved by a simple least square inversion:

524 $\tau = (A^T A)^{-1} A^T \delta\tau$

525 where τ is now the relative phase delay of all the stations compare to the reference station. τ and
526 the amplitude measurements we perform in Section 2.2 can then be used as the input for TPWM.

527 6 CONCLUSION

528 In this study, a new method to measure the surface wave phase velocity is described in detail. This
529 method is based on the cross-correlation of waveforms from nearby stations to obtain the phase
530 variations between station pairs. We find that the cross-correlation measurement is more robust
531 than the conventional FTAN measurement under the influence of random noise.

532 The phase variation and amplitude measurements are inverted for the phase velocity using
533 Helmholtz equation. With the coherence and other data quality estimations serving as selection
534 criteria, we are able to build an automated system that retrieves phase velocity maps directly from
535 seismic raw data without any manual interactions. We tested this system on the USArray data and
536 provide robust and up-to-date phase velocity maps for Rayleigh waves. 

537 The Love wave results are also calculated. However, we find that the overtones interference
538 generates systemic bias in the Love wave phase velocity results. Further study is under-going to
539 investigate this phenomenon.

540  The 2D spectral analysis of the Rayleigh wave phase velocity maps indicates interesting con-

541 trast between the tectonic active western US and the stable eastern US. The phase velocity vari-
 542 ations in the western US are significantly greater than those in the eastern US at most of the
 543 structural wavelengths.

544 The phase velocity maps presented in this study are weekly updated and available at: <https://www.ledo.columbia.edu/~ge.jin/projects/USarray.html>. The Matlab code of the auto-
 545 mated surface wave measuring system (ASWMS) is available at <https://github.com/jinwar/matgsdf>.

548 ACKNOWLEDGMENTS

549 Some NSF fund, Jiayin Xie, Fan-chi Lin, Göran Ekström, Anna Foster.

550 REFERENCES

- 551 Bensen, G.D., Ritzwoller, M.H., Barmin, M.P., Levshin, A.L., Lin, F., Moschetti, M.P., Chapiro, N.M. &
 552 Yang Y., 2007. Processing seismic ambient noise data to obtain reliable broadband surface wave disper-
 553 sion measurements. *Geophys. J. R. astr. Soc.*, , **169**, 12391260. doi:10.1111/j.1365-246X.2007.03374.x
- 554 Bodin, T., & Maupin, V., 2008. Resolution potential of surface wave phase velocity measurements at small
 555 arrays, *Geophys. J Int.*, , **172**, 698706.
- 556 Chen, P., Jordan, T.H., & Lee, E.J., 2010. Perturbation kernels for generalized seismological data functionals
 557 (GSDF), *Geophys. J Int.*, , **183**, 869-883.
- 558 Chen, P., Jordan, T. H., & Zhao, L., 2007. Full threedimensional tomography: a comparison between the
 559 scatteringintegral and adjointwavefield methods, *Geophys. J Int.*, , **170**, 175-181.
- 560 Chen, P., Zhao, L., & Jordan, T.H., 2007. Full 3D tomography for the crustal structure of the Los Angeles
 561 region, *Bull. seism. Soc. Am.*, , **97**, 1094-1120.
- 562 Dziewoński, A.M., Lekic, V., & Romanowicz, B.A., 2010. Mantle Anchor Structure: An argument for
 563 bottom up tectonics, *Earth Planet. Sci. Lett.*, , **299**, 6979. doi:10.1016/j.epsl.2010.08.013
- 564 Eddy, C. L. & Ekström G., 2013. Local amplification of Rayleigh waves in the continental United States
 565 observed on the USArray, *Earth Planet. Sci. Lett.*, in press, DOI: 10.1016/j.epsl.2014.01.013.
- 566 Ekström, G., Tromp, J., & Larson, E.W.F., 1997. Measurements and global models of surface wave propa-
 567 gation. *J. geophys. Res.*, , **102**, 8137-8157.
- 568 Ekström, G., 2013. Love and Rayleigh phase-velocity maps, 5-40s, of the western and central USA from
 569 USArray data, *Earth Planet. Sci. Lett.*, , **in press**.
- 570 Forsyth, D. W., & Li, A., 2005. Array analysis of two-dimensional variations in surface wave phase velocity

- 571 and azimuthal anisotropy in the presence of multipathing interference, *Geophysical Monograph Series*,
 572 **157**, 81-97.
- 573 Foster, A., Ekström, G., Nettles, M., 2014. Surface-wave phase velocities of the western United States from
 574 a two-station method. *Geophys. J Int.*, **196**, 11891206.
- 575 Foster, A., Ekström, G., Nettles, M., 2014. Overtones interference of Love wave. *Bull. seism. Soc. Am.*, **in**
 576 **press**.
- 577 Friederich, W., & Wielandt E., 1995. Interpretation of Seismic Surface Waves in Regional Networks: Joint
 578 Estimation of Wavefield Geometry and Local Phase Velocity. Method and Numerical Tests, *Geophys. J. R. astr. Soc.*, **120**, 731-744.
- 580 Gaherty, J.B., 2001. Seismic evidence for hotspot-induced buoyant flow beneath the Reykjanes Ridge, *Science*, **293**, 1645-1647.
- 582 Gaherty, J.B., 2004. A surface wave analysis of seismic anisotropy beneath eastern North America, *Geophys. J Int.*, **158**, 1053-1066.
- 584 Gaherty, J.B., & Dunn, R.A., 2007. Evaluating hot spotridge interaction in the Atlantic from regionalscale
 585 seismic observations, *Geochemistry, Geophysics, Geosystems*, 8.
- 586 Gaherty, J.B., & Jordan, T.H., 1995. Lehmann discontinuity as the base of an anisotropic layer beneath
 587 continents, *Science*, **268**, 1468-1471.
- 588 Gaherty, J. B., Jordan, T. H., & Gee, L. S. (1996). Seismic structure of the upper mantle in a central Pacific
 589 corridor, *J. geophys. Res.*, **101**, 22291-22309.
- 590 Gee, L.S., & Jordan, T.H., 1992. Generalized seismological data functionals, *Geophys. J Int.*, **111**, 363-390.
- 591 Levshin, A.L., & Ritzwoller, M.H., 2001. Automated detection, extraction, and measurement of regional
 592 surface waves, *Pure. appl. geophys.*, **158**, 1531-1545.
- 593 Levshin, A., Ratnikova, L., & Berger, J, 1992. Peculiarities of surface-wave propagation across central
 594 Eurasia, *Bull. seism. Soc. Am.*, **82**, 2464-2493.
- 595 Li, X.D., & Romanowicz, B, 1996. Global mantle shear velocity model developed using nonlinear asymptotic
 596 coupling theory, *J. geophys. Res.*, **101**, 22245-22272.
- 597 Lin, F.C., & Ritzwoller, M.H., 2011. Helmholtz surface wave tomography for isotropic and azimuthally
 598 anisotropic structure, *Geophys. J Int.*, **186**, 1104-1120.
- 599 Lin, F.C., Ritzwoller, M.H., & Snieder, R., 2009. Eikonal tomography: surface wave tomography by phase
 600 front tracking across a regional broad-band seismic array, *Geophys. J Int.*, **177**, 1091-1110.
- 601 Lin, F.C., Tsai, V.C., & Ritzwoller, M.H., 2012. The local amplification of surface waves: A new observable
 602 to constrain elastic velocities, density, and anelastic attenuation, *J. geophys. Res.*, **117**, B06302.
- 603 Nettles, M., & Dziewoski, A. M. (2011). Effect of Higher-Mode Interference on Measurements and
 604 Models of Fundamental-Mode Surface-Wave Dispersion. *Bull. seism. Soc. Am.*, **101**, 2270-2280.
 605 doi:10.1785/0120110019

- 606 Owens, T.J., Crotwell, H.P., Groves, C., & Oliver-Paul, P., 2004. SOD: Standing order for data, *Seism. Res.*
607 *Lett.*, **75**, 515-520.
- 608 Rau, C. J., & Forsyth, D.W., 2011. Melt in the mantle beneath the amagmatic zone, southern Nevada,
609 *Geology*, **39**, 975-978.
- 610 Schaff, D.P., & Beroza, G.C., 2004. Coseismic and postseismic velocity changes measured by repeating
611 earthquakes, *J. geophys. Res.*, **109**.
- 612 Tape, C., Liu, Q., Maggi, A., & Tromp, J., 2010. Seismic tomography of the southern California crust based
613 on spectral-element and adjoint methods, *Geophys. J Int.*, **180**, 433-462.
- 614 VanDecar, J.C., & Crosson, R.S., 1990. Determination of teleseismic relative phase arrival times using
615 multi-channel cross-correlation and least squares, *Bull. seism. Soc. Am.*, **80**, 150-169.
- 616 Wielandt, E., 1993. Propagation and Structural Interpretation of NonPlane Waves, *Geophys. J Int.*, **113**,
617 45-53.
- 618 Yang, Y., & Forsyth, D. W., 2006. Regional tomographic inversion of the amplitude and phase of Rayleigh
619 waves with 2-D sensitivity kernels, *Geophys. J Int.*, **166**, 1148-1160.
- 620 Yang, Y., Shen, W., & Ritzwoller, M.H., 2011. Surface wave tomography on a large-scale seismic array
621 combining ambient noise and teleseismic earthquake data, *Earthquake Science* **24**, 55-64.
- 622 Shen, W., Ritzwoller, M. H., & Schulte?Pelkum, V., 2013. A 3?D model of the crust and uppermost mantle
623 beneath the Central and Western US by joint inversion of receiver functions and surface wave dispersion,
624 *J. geophys. Res.*, **118**, 262276, doi:10.1029/2012JB009602.
- 625 Zhu, H., Bozda? E., Peter, D., & Tromp, J., 2012. Structure of the European upper mantle revealed by
626 adjoint tomography, *Nature Geoscience*, **5**, 493-498.

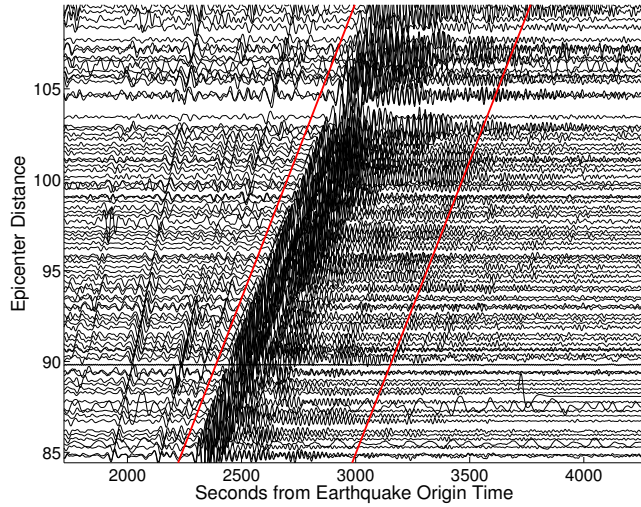


Figure 1. USarray vertical component records for the January 18th, 2009 earthquake near Kermadec Islands, New Zealand ($M_w=6.4$). Red lines show the window function W_S to isolate the fundamental Rayleigh wave energy, which is automatically generated. The length and amplitude variation of the coda demonstrates the scattering effect caused by local heterogeneities.

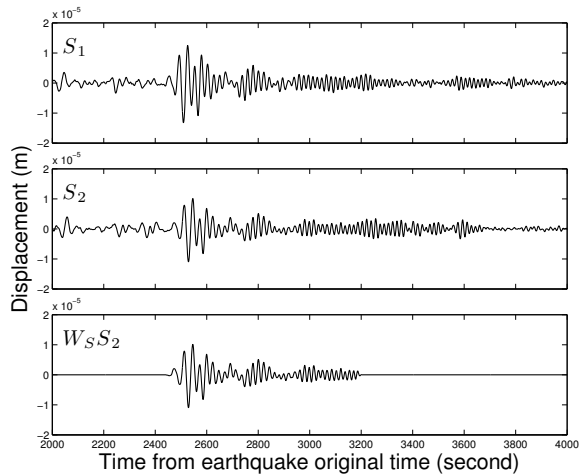


Figure 2. Sample waveforms of a nearby station pair for the same earthquake as in Fig.1. Record S_1 is from station W17A, and record S_2 is from station W18A. The two stations are 89 km apart and have the almost identical waveforms. The lower panel demonstrates the effect of the window function W_S , which is applied to isolate the energy of fundamental Rayleigh wave.

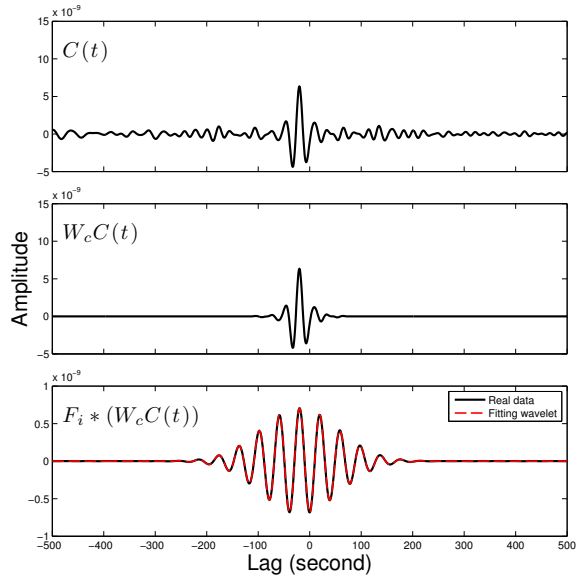


Figure 3. The cross-correlation procedures for the waveforms shown in Fig. 2. Top: cross-correlating the waveforms from the two stations. Middle: windowing the cross-correlograms around the maximum amplitude. Bottom: applying the narrow-band filter (25 mHz) and fitting the five-parameter wavelet.

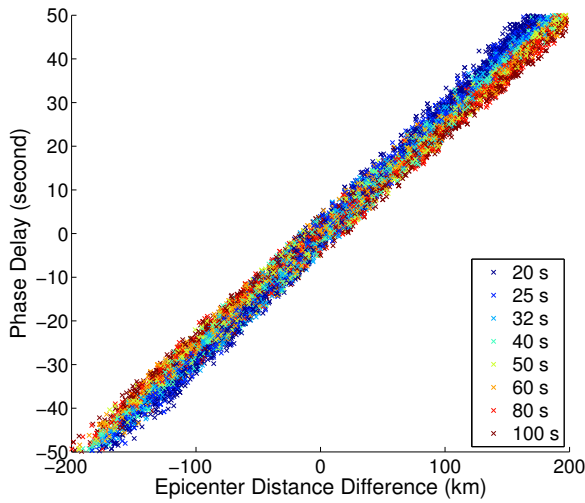


Figure 4. Relative phase delays against epicenter distance differences of all the station pairs within 200 km for the same records shown in Fig. 1. Crosses with different color represent the measurements at different frequencies. An increasing move-out at lower frequencies can be observed, which demonstrates the average phase velocity dispersion of Rayleigh wave across the array.

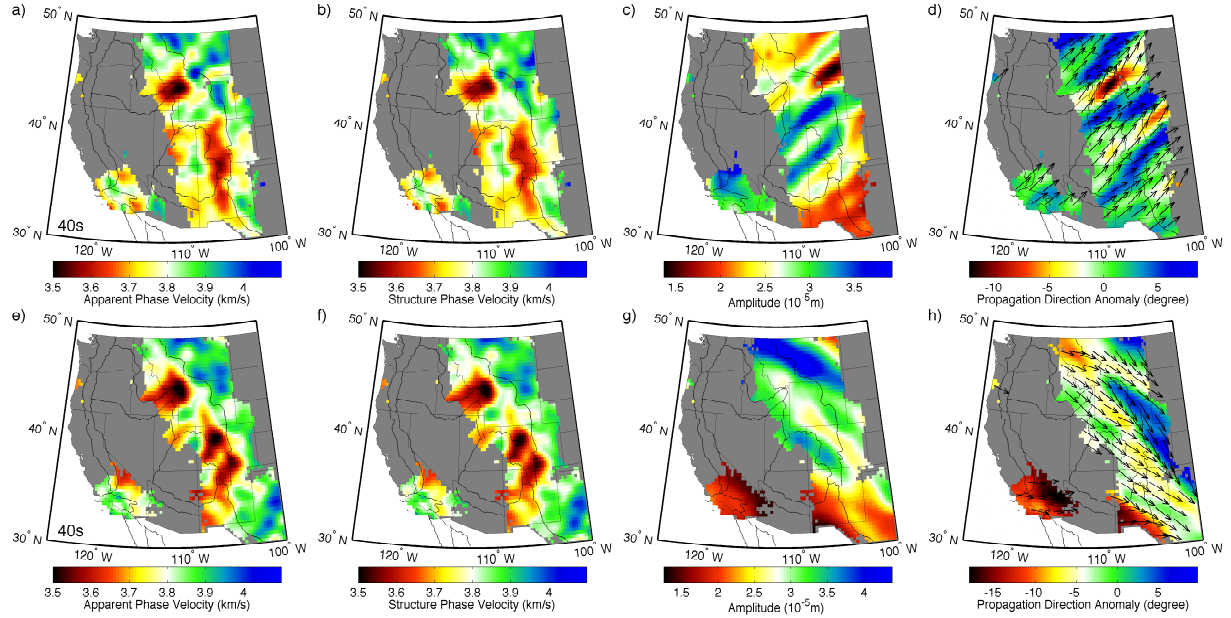


Figure 5. The 40 s Rayleigh wave results for two earthquakes. **a)** The apparent phase velocity map derived from phase delay measurements (Fig. 4) for the same earthquake as shown in Fig. 1. **b)** The corrected phase velocity map derived from the apparent phase velocity and amplitude measurements using Helmholtz equation. **c)** The amplitude map for the same earthquake. **d)** The surface wave propagation direction anomaly map. The arrows point to the propagation direction while the color contour illustrates the angle differ from the great circle path. The rotation of arrows from the great circle path is exaggerated by three times for demonstration. **e)-h)** Same as a)-d) but for the April 7, 2009 earthquake near Kuril Islands ($M_s = 6.8$).

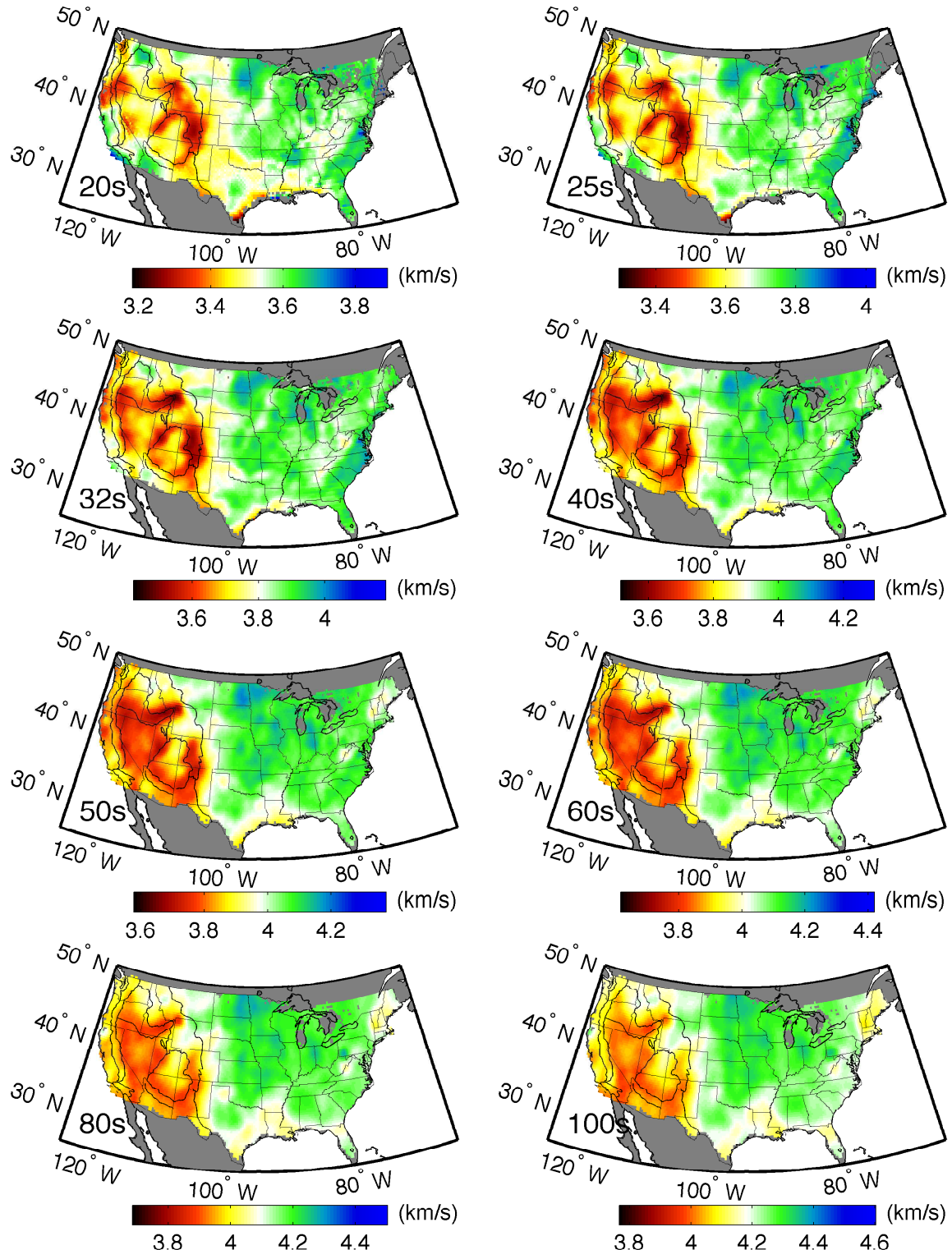


Figure 6. Rayleigh wave phase velocity maps at different frequencies. This result is updated on ???, 2014, with totally ??? events being stacked. The weekly updated result can be found at: <http://www.1deo.columbia.edu/~ge.jin/projects/maps/rayleigh.html>

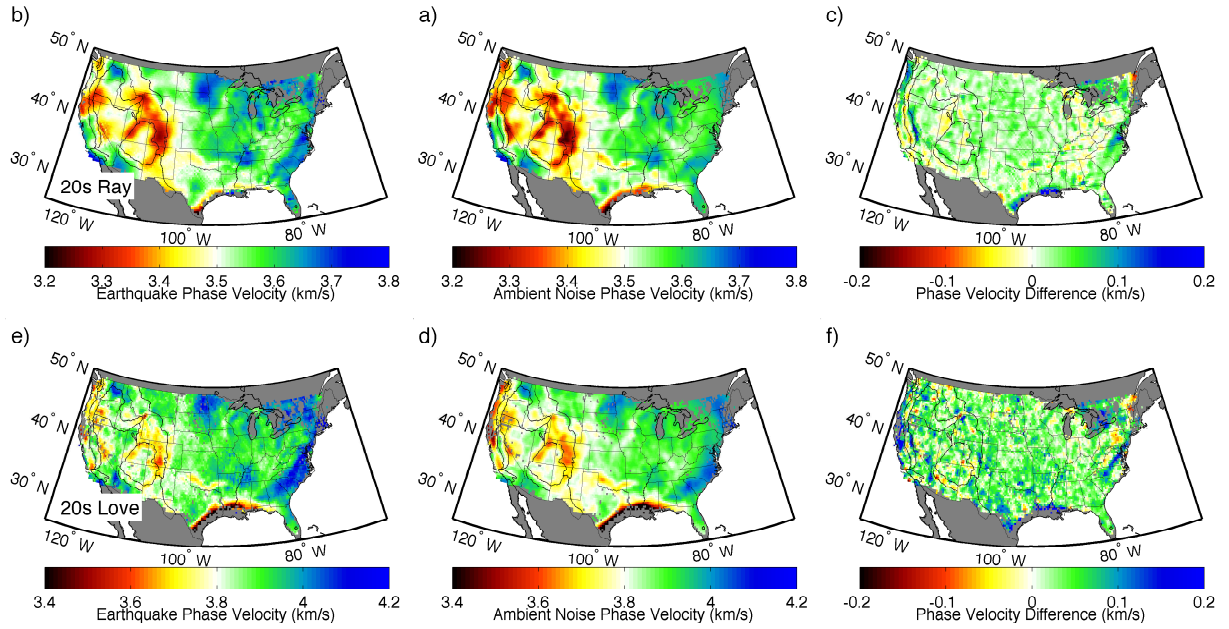


Figure 7. 20 s Rayleigh and Love wave phase velocity comparison between the earthquake (this study) and the ambient noise (Ekström 2013) results.

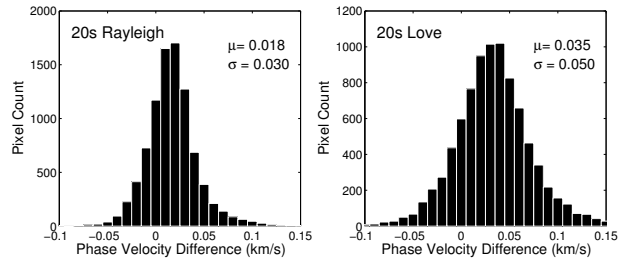


Figure 8. Histograms of phase velocity difference between the maps shown in Fig. 7.

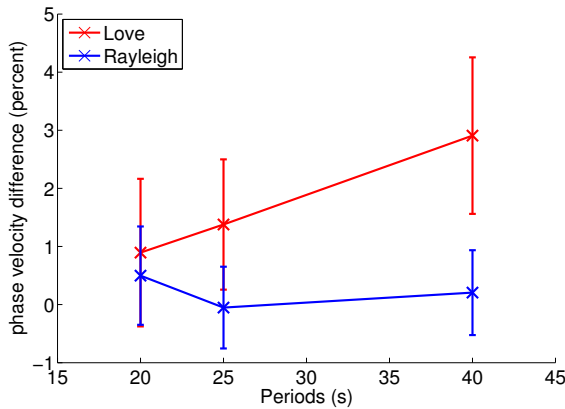


Figure 9. The means and standard deviations of the phase velocity difference between earthquake measurement (this study) and ambient noise measurement (Ekström 2013) at different periods. Rayleigh wave results show good agreements between the two studies, while Love wave results indicate a systemic bias increasing with period.

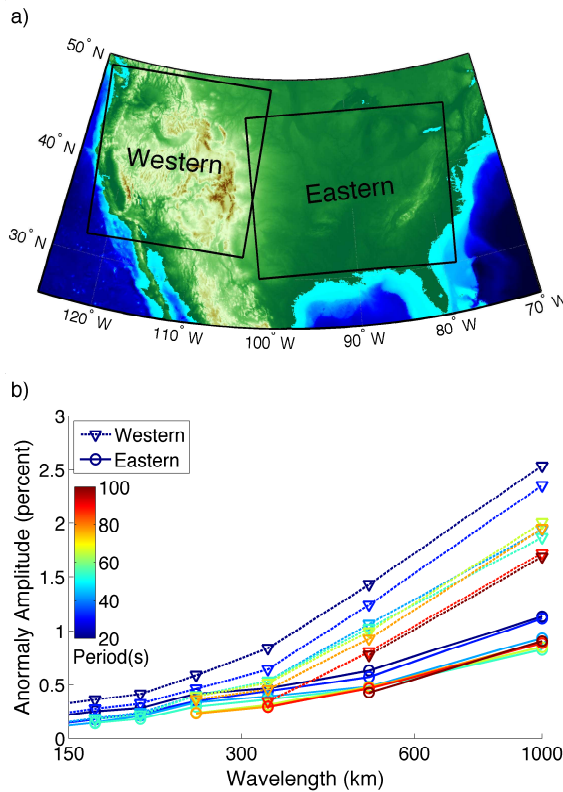


Figure 10. 2D Fourier analysis on the phase velocity maps for Rayleigh Wave. a) Regions that being analyzed. b) Magnitude of phase velocity variation against structural wavelength at different frequency bands. Only the structural wavelengths larger than the surface wave wavelength are plotted.

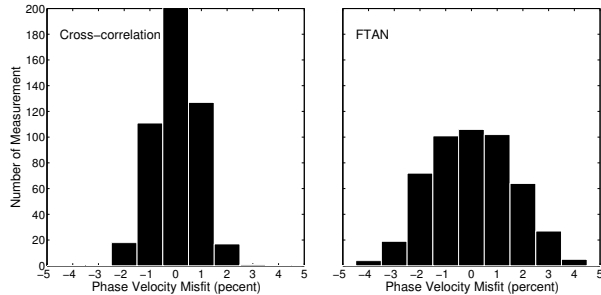


Figure 11. Comparison between cross-correlation measurements and FTAN measurements in a 1D synthetic test. Left panel: the misfit histogram of our method for 200 independent measurements under 20% noise level. Right panel: the misfit of FTAN measurement on the same dataset.

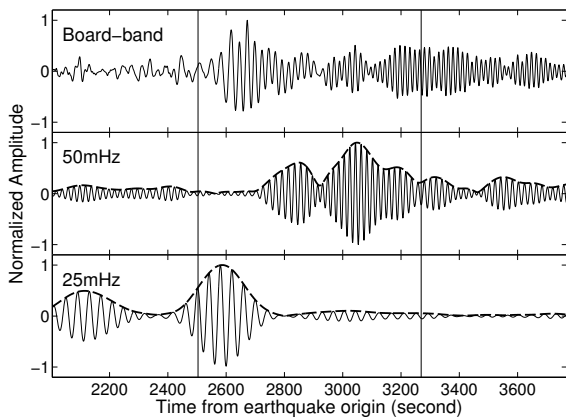


Figure 12. Station 327A vertical component record for the same earthquake as in Fig. 1. Upper panel: the original waveform filtered from 5 mHz to 100 mHz. Middle and lower panels: narrow-band filtered waveform with the center frequency of 50 mHz and 25 mHz respectively. Thick dash lines are the envelop functions, the vertical thin lines show the location of isolation window function W_S . FTAN method is difficult to make robust measurements at high frequencies as the selection of group delay can be controversial.

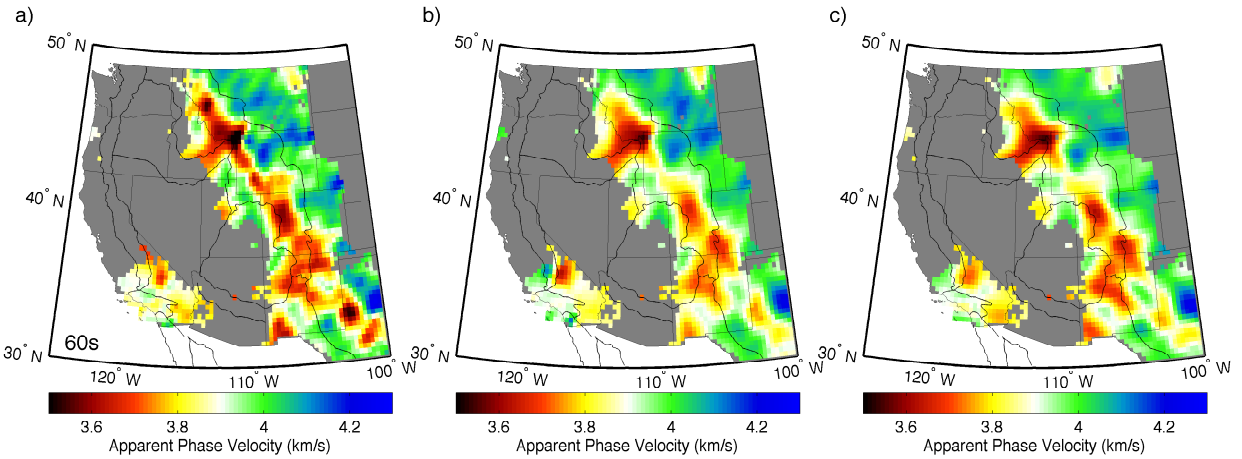


Figure 13. 60 s Rayleigh wave Eikonal tomography results for the April 7, 2009 earthquake near Kuril Islands ($M_s=6.8$), using different phase measurement methods and Eikonal tomography inversions. We select the same earthquake as shown in fig. 3a of Lin and Ritzwoller (2011) for comparison. a) Phase velocity obtained by using the FTAN phase measurement, and taking the gradient of travel-time surface. b) Same as a) but using cross-correlation phase measurement. c) Same as b) but phase velocity is obtained by inverting slowness vector.

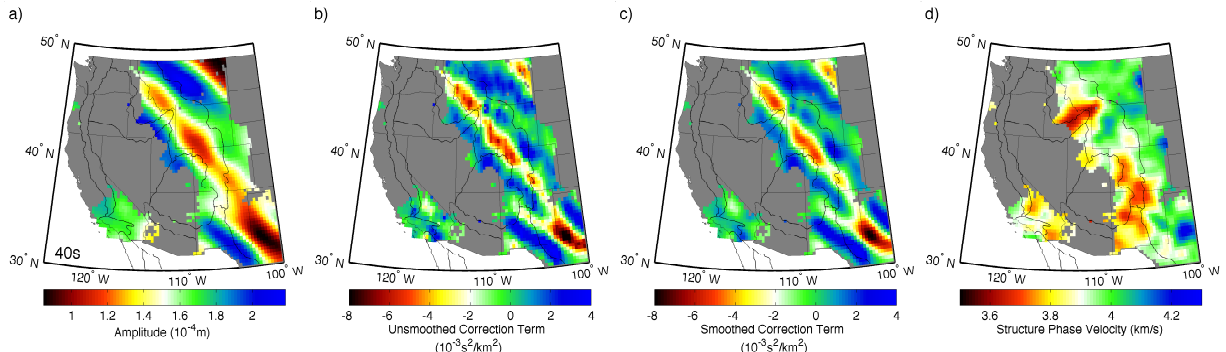


Figure 14. Demonstration of the amplitude correction procedure on the apparent phase velocity map in Fig. 13c. **a)** The amplitude map generated by fitting minimum curvature surface. **b)** The preliminary correction term derived from a). **c)** The smoothed correction term. **d)** The corrected phase velocity map, derived from c) and Fig. 13c.